Prediction of Optimal Synthesis Conditions for the Formation of Ordered Double-Transition-Metal MXenes (o–MXenes)

Nuala M. Caffrey*

School of Physics, University College Dublin, Dublin 4, Ireland

E-mail: nuala.caffrey@ucd.ie

Abstract

o–MXenes are a family of layered double-transition metal carbides and nitrides with a unique out-of-plane ordering of the two metal atoms. Their chemical versatility means they have novel applications in energy storage, catalysis and sensing devices. o–MXenes are synthesized from their precursor o–MAX phase materials using a chemical etching process, although yields are typically low. The optimal conditions necessary for the etching of MAX phase materials can be predicted using Pourbaix diagrams. Here, Pourbaix diagrams produced from first-principles calculations are used to determine the conditions necessary to enhance the yields of o–MXenes. In agreement with experiment, we show that high yields of (Mo, Ti)$_2$CT_x are possible, as the o–MXene is stable relative to known competing ionic and molecular species in an aqueous solution across a wide range of pH and applied potentials. We show how the stability of the o–MXene depends on the nature of the terminating groups and the presence of metal vacancies on the o–MXene surface.

Introduction

$M_{n+1}AX_n$, or MAX, phases are layered, hexagonal, early transition-metal carbides and nitrides, where M is an early transition metal, A is an A-group element (mostly Groups 13 and 14), X is C and/or N, and $n = 1$, 2, 3 or more recently 4.[1] MAX phases have found uses in diverse applications as they combine both ceramic and metallic attributes, and are particularly suited to high-temperature applications such as electronic contacts and protective coatings. They are also precursors to MXenes, their two-dimensional (2D) counterparts.[2–4] These are produced by selectively chemically etching the A elements from the parent MAX phase using, typically, an aqueous HF solution. The acid attacks the M-A bonds, forming A-F_x compounds which diffuse out. The MXene layers are immediately passivated by a mixture of oxygen, fluorine and hydroxyl terminating groups (T). Driven by their huge chemical versatility, these 2D layered materials have found applications in energy storage,[5] catalysis[6,7] and sensing.[8]

This versatility can be increased even further by considering solid solutions of two or more metal atoms on the M site. In some cases, the metal atoms exhibit spontaneous ordering, with both in-plane (i–MAX) and out-of-plane (o–MAX) ordering observed and characterized.[9] The general formula of all known o–MAX phases is (M′, M″)$_{n+1}$AlC$_n$, where M′ and M″ denote early transition metals and n is either 2 or 3. The ordering is such that two M′ layers 'sandwich' either one or two layers of M″ within each M-X block. The first o–MAX phase was discovered in 2014 by Liu and coworkers[10,11] who synthesized Cr_2TiAlC_2. Shortly thereafter, Caspi and coworkers[12] synthesized $(Cr_{0.5}V_{0.5})_{n+1}AlC_n$ with $n = 2$ and 3. In 2015, Mo_2TiAlC_2 and $Mo_2Ti_2AlC_3$ were synthesized, exhibiting for the first time Mo - Al bonds.[13,14] More recently, Mo_2ScAlC_2 was successfully synthesized.[15] Experimental synthesis has been limited so far to these six phases, but several more have been predicted to be stable.[16,17]

The metal ordering in most of these o–MAX materials is not perfect, with both experimental and computational evidence that some M′ and M″ atoms exchange positions. While the inner layers are typically comprised of 100% M″ atoms, the outer layers are also occupied by some M″ atoms. This is the case for $(Cr_{0.5}V_{0.5})_3AlC_2$, where Rietveld analysis of neutron diffraction data showed that the inner layer is comprised of 100% V atoms, while the outer layers consisted of approximately 75% Cr atoms and 25% V atoms.[12] Similarly, in Mo_2TiAlC_2 the outer layers were found to consist of 75% Mo and 25% Ti, while the inner layers were occupied by Ti alone.[13] Meshkian et al. also observed partial intermixing between the M elements in Mo_2ScAlC_2.[15] Finally, while the authors do not report on the degree of ordering, there is some speculation that Cr_2TiAlC_2 also has an incomplete ordering of the metal atoms with some fraction of the Ti atoms occupying the Cr sites.[9] The preference for a particular (M′, M″) chemistry to result in an ordered o–MAX phase rather than a disordered solid solution was shown by Dahlqvist

et al. to occur if the two metal atoms are of similar size, with a large difference in their electronegativity, and if the metal atom next to the Al-layer does not form a stable binary rock-salt structure.[17]

o–MAX phases are particularly interesting as they are potential precursors for *o*–MXenes with surface layers that could not be obtained otherwise. For example, Cr-based MXenes were proposed to improve energy storage and catalysis applications,[18–20] but as neither the etching of Cr_2AlC nor the synthesis of Cr_3AlC_2 was possible, experimental verification was unobtainable until $(Cr_{2/3}Ti_{1/3})_3AlC_2$ was etched to produce flakes with surface Cr atoms.[3,21] $(Cr_{0.5}V_{0.5})_3AlC_2$ and Mo_2ScAlC_2 have also both been etched to produce their associated *o*–MXenes, although some residual MAX phase is still present after the etching procedure.[2] For the case of Mo_2ScAlC_2, ScF_3 particles are also present in the solution, suggesting that Sc, potentially present in the surface due to interlayer mixing, is also partially etched.[15] The etching of Mo_2TiAlC_2 is more effective, with a 100% *o*–MXene yield achieved.[3,22] Depending on the chemistry, etching times between 16 and 69 hours and etching temperatures ranging between room temperature and 55°C were required.

Here, we predict the optimal synthesis conditions for the formation of several *o*–MXene 2D materials and determine the solution conditions necessary to maximize their yields. Using density functional theory calculations, we investigate how effective acid etching is on the known 312 double transition metal MAX phase materials, namely (Cr, Ti)$_3$AlC$_2$, (Cr, V)$_3$AlC$_2$, (Mo, Ti)$_3$AlC$_2$ and (Mo, Sc)$_3$AlC$_2$. We construct 'etching' Pourbaix diagrams, which show the stability of the *o*–MAX and *o*–MXene phases relative to known competing ionic and molecular species that may form in aqueous solution as a function of pH and potential. In particular, we examine how the nature of the *o*–MXene terminating groups, the experimentally observed interlayer mixing of the metal atoms, and the presence of metal vacancies all play a role in stabilizing the resulting *o*–MXenes.

Computational Details

Construction of Etching Pourbaix Diagrams

Pourbaix diagrams were constructed following the formalism initially developed by Persson et al.[23] and which was extended by Ashton et al.[24] to consider specifically 'etching' diagrams. An implementation of MP-Interfaces[25,26] is used. The procedure is summarized here: For all relevant compounds and ionic species, a free energy of formation can be determined as:

$$\Delta G(\phi, \mathrm{pH}) = \Delta G^0 + 2.303\,RT\,\log c_i - N_O\,\mu_{\mathrm{H_2O}} - 2.303\,RT\,(2N_O - N_H)\,\mathrm{pH} - (2N_O - N_H + m)\phi$$

where ϕ is the electrochemical potential, ΔG^0 is the free energy of formation at standard conditions, c_i is the concentration of the species (taken as 1 M for solid materials, and 10^{-3} M for all ionic species in solution), R is the ideal gas constant, T is the temperature (taken as room temperature), N_O and N_H are the number of oxygen and hydrogen atoms, respectively, $\mu_{\mathrm{H_2O}}$ is the chemical potential of water (taken as -2.46 eV), and m is the charge of the species.

The thermodynamically favoured structure is determined by minimization of $\Delta G(\phi, \mathrm{pH})$ among the set of all possible solid phases (subject to compositional constraints for the multi-element *o*–MAX phase materials considered here) and dissolved species. A Pourbaix diagram is then constructed as the convex hull connecting the formation energies of all relevant compounds and ionic species. Only the *o*–MAX and *o*–MXene solid phases are considered. The standard hydrogen electrode (SHE) is used as the potential reference.

Density Functional Theory

The formation energies of the solid phases (*o*–MAX phases and multi-layered *o*–MXenes) are determined within the framework of density functional theory (DFT), using the projector augmented wave method as implemented in the Vienna ab initio simulation package VASP code.[27–29] The exchange-correlation functional of Perdew-Burke-Ernzerhof (PBE) is employed.[30] The DFT-D3 method with Becke-Johnson (BJ) damping is used to account for dispersion interactions.[31] The plane-wave energy cutoff is converged using a 520 eV energy cutoff. A $5 \times 5 \times 3$ and $23 \times 23 \times 7$ Monkhorst-Pack k-point grids[32] are used during structural optimization and DOS calculations, respectively, for a 2×2 unit cell. The structures are fully optimized with a maximum force criterion of 10^{-2} eV/Å. Spin polarized calculations for performed for Cr-based compounds. The formation energies are defined relative to the elemental phases of all involved species. For elements that are gaseous at standard conditions, namely oxygen and flourine, the entropic contributions to the Gibbs free energy cannot be neglected. This correction is taken from NIST-JANAF Thermochemical Tables.[33] The entropic contributions to the energies of the solid phase species are much smaller than those of the gas phases and so are neglected.

Calculating the formation energies for ions and molecules in solution is difficult. Instead, following the procedure of Persson et al.,[23] the experimental formation energies of all possible neutral and charged molecules comprised of each of the M, A and X elements combined with –O, –H, –F or –O–H atoms are extracted from the NIST NBS tables[34] and Pourbaix's Atlas.[35] A correction is then applied to these experimental formation energies, given by the difference between the DFT and experimental formation energies of a reference compound, such as a simple binary oxide. For example, the experimental formation energies of Ti^{2+}, Ti^{3+} and

TiO_2^{2+} are corrected by an amount:

$$\Delta\mu_{\mathrm{Ti}}^{\mathrm{correction}} = E_f^{\mathrm{DFT}}(\mathrm{TiO_2}) - E_f^{\mathrm{exp}}(\mathrm{TiO_2})$$

which is applied additively for each atom in the considered species.

The potential of zero charge (PZC) is the electric potential of a neutral electrode surface in solution. If there is a non-zero PZC, local potentials will be present at the surface which will affect the etching process. The PZC is determined using an implicit solvent model, as implemented in VASPsol[36,37] and is given relative to the SHE (determined as 4.6 V[38]). The surface is modelled as an o–MAX slab of 11 atomic layers with a thick vacuum layer of approximately 20 Å in the direction normal to the slab surface. The solvent is modelled with an aqueous electrolyte permittivity, ϵ_r, of 78.4, and a Debye length of 2 Å. The PZC is then given by the difference between the potential in the bulk of the solvent and the Fermi level of the slab. The former is obtained by calculating the planar average of the electrostatic potential across the super-cell and taking the potential sufficiently far from the surface along the surface normal direction.

Interlayer mixing is taken into account in a 2×2 unit cell by replacing one M′ in each outer layer with an M″ atom, resulting in an $(M'_{0.5}M''_{0.5})_3AlC_2$ stoichiometry. There is some evidence that vacancies, either individual or ordered, can occur in o–MXenes after etching.[39,40] Here, we consider single vacancies by removing one M′ atom from the surface layer in the same 2×2 unit cell. This results in a $(M'_{0.5}M''_{0.3})_3AlC_2$ stoichiometry. Representative o–MAX and o–MXene structures are shown in Fig. 1(a) and (b), respectively.

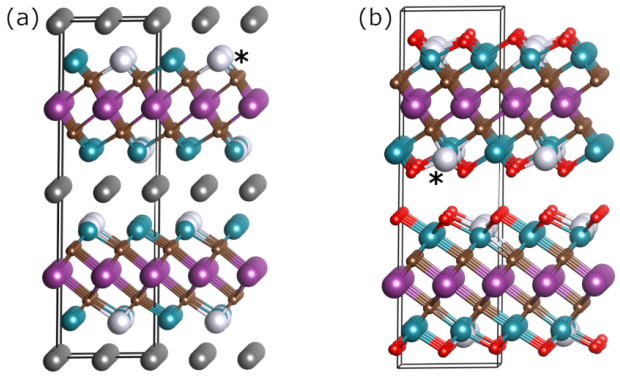

Figure 1: (a) $(M', M'')_3AlC_2$ o–MAX phase material. (b) $(M', M'')_3C_2O_2$ o–MXene material. Green spheres represent M′ atoms, purple spheres represent M″ atoms, brown spheres represent carbon atoms and grey spheres represent aluminium atoms. White atoms (marked with star symbol): If interlayer mixing is not considered, this is an M′ atom. If interlayer mixing is considered this is an M″ atom, resulting in a $(M'_{0.5}M''_{0.5})_3AlC_2$ o–MAX stoichiometry. If vacancies are considered this atom is removed, resulting in a $(M'_{0.5}M''_{0.3})_3AlC_2$ o–MAX stoichiometry.

Results & Discussion

No interlayer mixing of M′ and M″ atoms

We start by assuming there is no interlayer mixing present, i.e., by assuming 100% of the M′ atoms occupy the outer layers, and 100% of the M″ atoms occupy the interior positions in the M-X block. This will allow us to isolate the effect of interlayer mixing on the ability to etch an o–MAX material to an o–MXene.

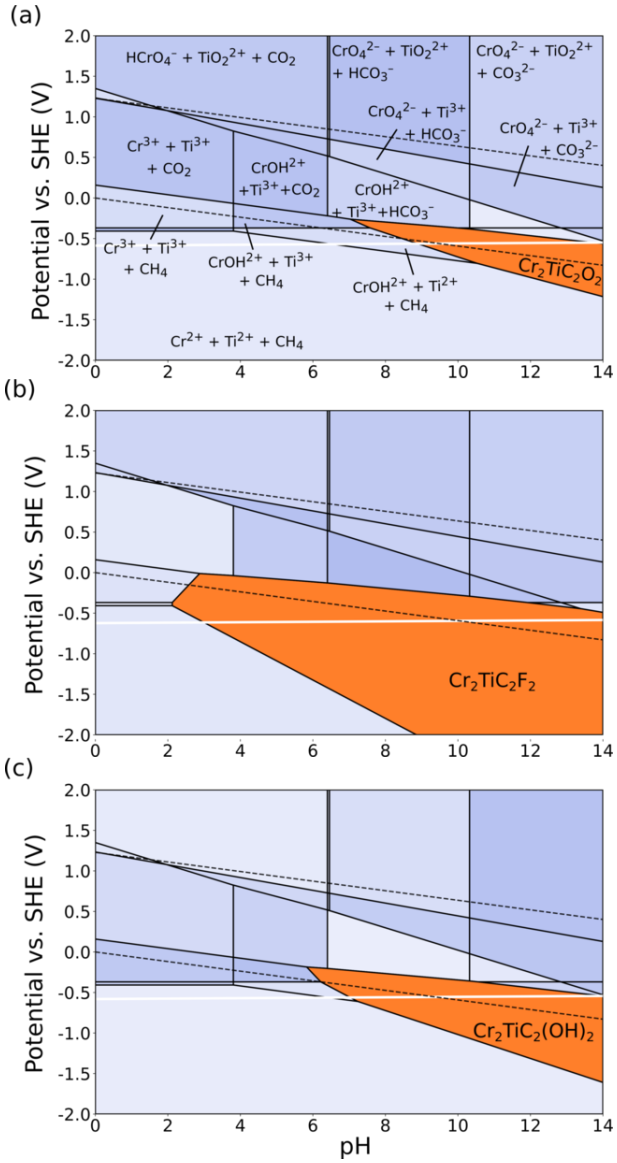

Figure 2: Etching Pourbaix diagram for Cr_2TiAlC_2, showing regions where (a) $Cr_2TiC_2O_2$ (b) $Cr_2TiC_2F_2$ and (c) $Cr_2TiC_2(OH)_2$ are stable (orange segments). The dashed black lines indicate the stability range of water. The solid white line shows the point of zero charge (PZC). Note that, for clarity, the ions which are present in solution are only shown for the –O terminated structure. They remain the same for the two other termination types.

The etching Pourbaix diagram of Cr_2TiAlC_2 is shown in Fig. 2. Etching into –O, –F and –OH terminated

o–MXenes are considered separately. Compared to Cr_2AlC which shows only a small region of stability for Cr_2CO_2 at pH > 9 as shown by Ashton et al.[24] and reproduced here (not shown), the stability region of the Cr-based o–MXene increases to pH > 7 (Fig. 2(a)). The potential of zero charge (PZC) is at -0.6 V vs. SHE, suggesting that etching will occur and result in a stable o–MXene, even without the application of an external potential. For pH values < 6.5 at PZC, the solid phases will dissolve in solution to form Cr^{2+} and Ti^{2+} ions (with CH_4 produced). At $6.5 >$ pH > 7, $CrOH^{2+}$ is more stable than Cr^{2+}.

Experimentally, HCl-LiF was used to etch this o–MAX phase material.[3] The availability of flourine would suggest that –F will be a significant component of the o–MXene terminating groups. Changing the surface termination type in this way will change the formation energy of the MXene phase, as well as the relativity stability of the dissolved ions in solution. The stability region of $Cr_2TiC_2F_2$ is shown in Fig. 2(b). It is significantly larger than that of $Cr_2TiC_2O_2$, reflecting the much higher formation energy of the –F terminated o–MXene (-8.7 eV/f.u. compared to -6.9 eV/f.u. for $Cr_2TiC_2O_2$). It is predicted to be stable in an aqueous solution over a wide range of pH, between 2 and 14.

Finally, the Pourbaix diagram of $Cr_2TiC_2(OH)_2$ is shown in Fig. 2(c). Compared to $Cr_2TiC_2O_2$, the region of stability of the –OH terminated o–MXene is slightly larger, extending into acidic pH values.

The etching diagram of Cr_2VAlC_2 is shown in Fig. 3. It is quite similar to that of Cr_2TiAlC_2. Here again, the stability region of the –O terminated o–MXene (Fig. 3(a)) is smallest, while the –F terminated o–MXene (Fig. 3(b)) is stable across essentially all pH values at negative potentials. As the PZC is -0.4 eV, $Cr_2VC_2F_2$ will be stable even without the application of an external potential. As shown in Fig. 3(c), higher pH values are required to stabilize $Cr_2VC_2(OH)_2$ compared to the –F terminated o–MXene. At lower pH, the solid phases dissolve in solution to form Cr^{3+} and VO^{2+} or $CrOH^{2+}$ and HVO_2^+ ions, depending on the pH.

The relative size of the area of stability in phase space for the three considered o–MXenes can be explained using their formation energies, namely -6.4eV, -8.1eV and -7.4eV/f.u. for the –O, –F and –OH terminated o–MXenes, respectively. The Cr-based dissolved phases are the same as for Cr_2TiAlC_2, while the V-based ions include VO^{2+} at low pH values, HVO_2^+ at intermediate pH values, and VO_4^{3-} at high values of pH. CH_4 is produced at negative applied external potentials. A caveat here is that interlayer mixing is not considered, yet significant intermixing is found experimentally. This will be addressed in the next section.

Whereas Cr_2TiAlC_2, for example, was found experimentally to be incompletely etched with approximately 20% Al remaining after the etching procedure, Mo_2TiAlC_2 was etched with 100% yield of the associated o–MXene.[3,22] This is consistent with the Pourbaix etching diagram, which shows a $Mo_2TiC_2T_2$ stability region extending across the entire pH range and for a wide range of negative potentials. This is shown in Fig. 4(a) and is particularly evident in the –O terminated o–MXene, which has a stability region significantly greater than that of $Cr_2TiC_2O_2$ or $Cr_2VC_2O_2$. Likewise, there are also increases in the areas of the stability regions of the –F and –OH terminated MXenes (Fig. 4(b) and (c), respectively). The stability of $Mo_2TiC_2F_2$ extends even into negative pH values. This higher stability is reflected in the formation energies of those MXenes, which range between -8.1 and -8.4 eV/f.u. In all cases, the ZPC lies within the stability region of the o–MXenes, suggesting that etching will occur without any external potential.

Finally, the Pourbaix diagram of Mo_2ScAlC_2 is shown

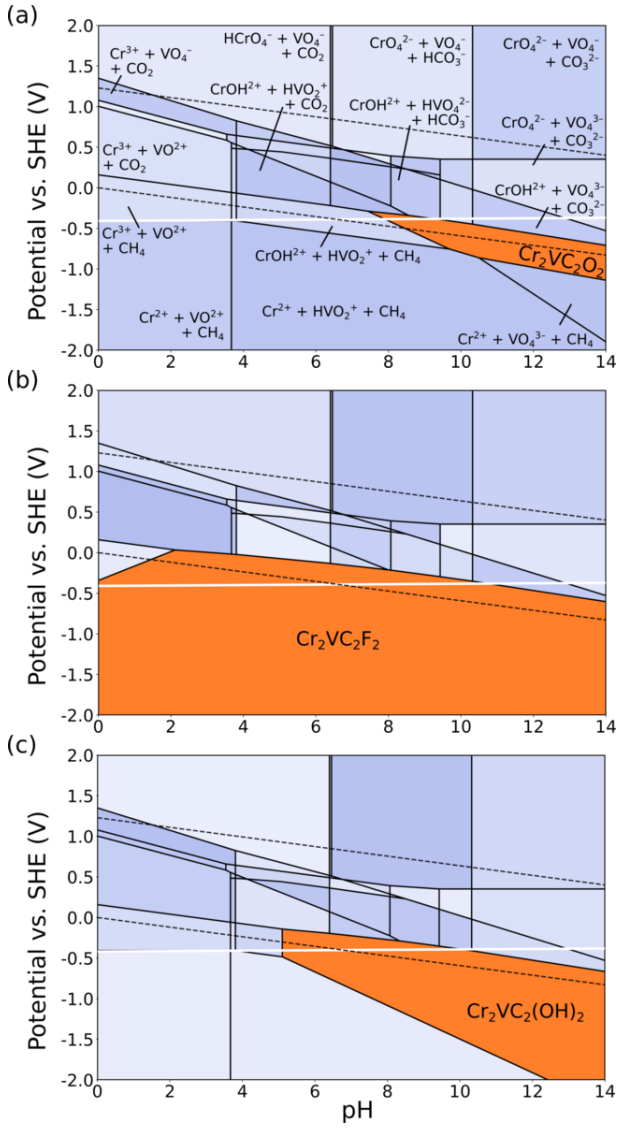

Figure 3: Etching Pourbaix diagram for Cr_2VAlC_2, showing regions where (a) $Cr_2VC_2O_2$ (b) $Cr_2VC_2F_2$ and (c) $Cr_2VC_2(OH)_2$ are stable (orange segments). The dashed black lines indicate the stability range of water. The solid white line shows the point of zero charge (PZC).

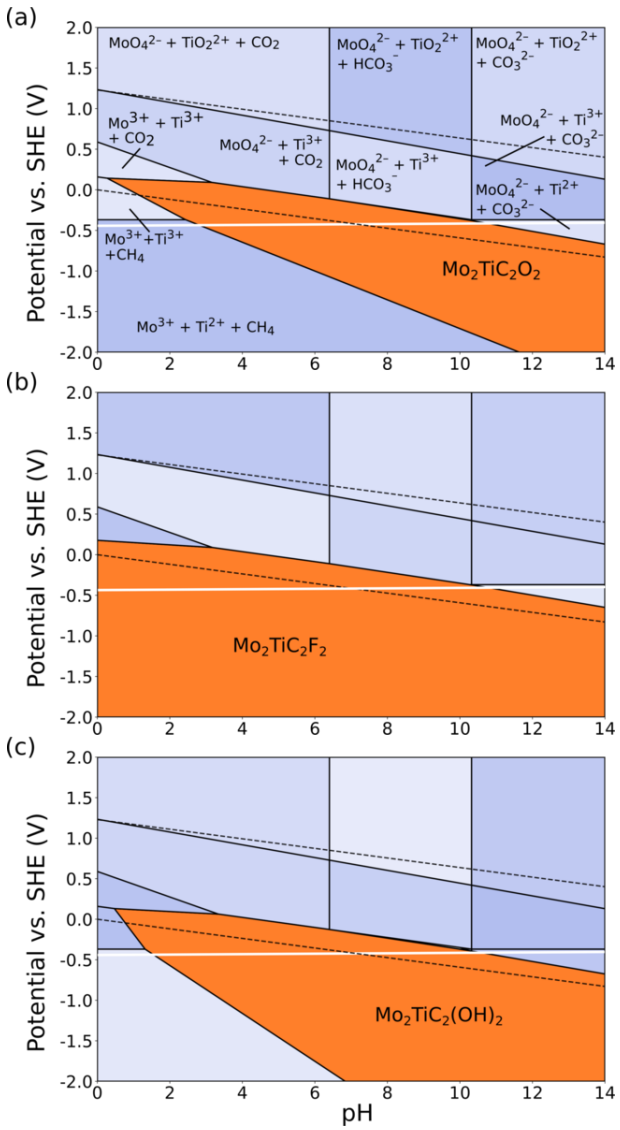

Figure 4: Etching Pourbaix diagram for Mo_2TiAlC_2, showing regions where (a) $Mo_2TiC_2O_2$ (b) $Mo_2TiC_2F_2$ and (c) $Mo_2TiC_2(OH)_2$ are stable (orange segments). The dashed black lines indicate the stability range of water. The solid white line shows the point of zero charge (PZC).

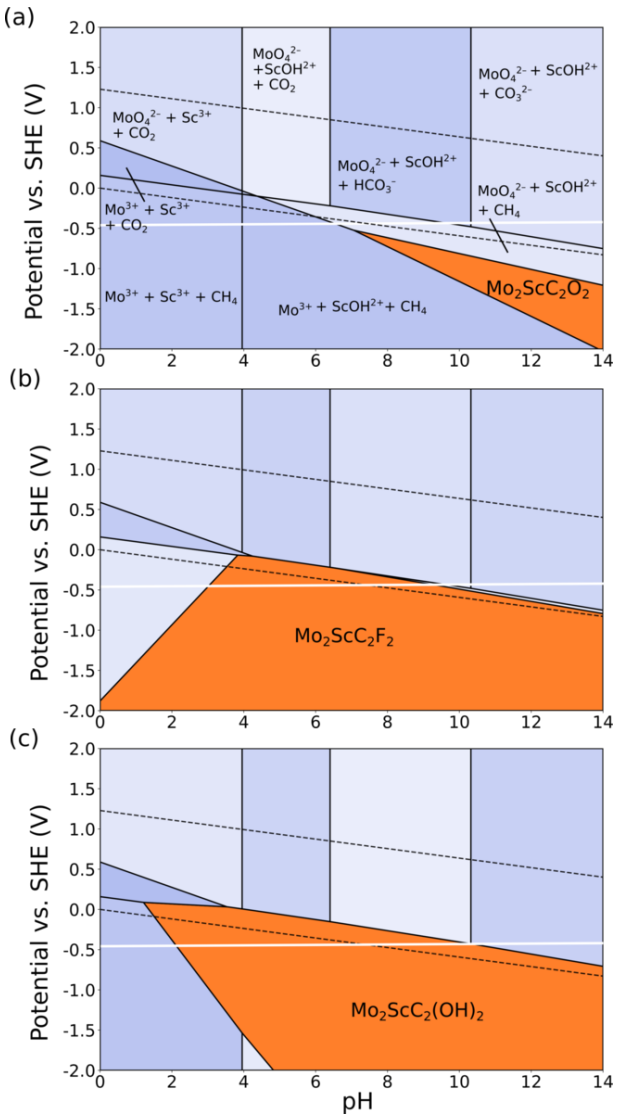

Figure 5: Etching Pourbaix diagram for Mo_2ScAlC_2, showing regions where (a) $Mo_2ScC_2O_2$ (b) $Mo_2ScC_2F_2$ and (c) $Mo_2ScC_2(OH)_2$ are stable (orange segments). The dashed black lines indicate the stability range of water. The solid white line shows the point of zero charge (PZC).

in Fig. 5. Compared to Mo_2TiAlC_2, the stability regions of the o–MXene phases are considerably smaller. Some of this difference can be accounted for by considering the lower formation energy of, for example, $Mo_2ScC_2O_2$ (by 0.6 eV/f.u.) compared to that of $Mo_2TiC_2O_2$. The higher formation energy of the ions also plays a role. For example, the formation energy of $ScOH^{2+}$ is -8.3eV and that of Sc^{3+} is -6.1eV, whereas the formation energy of Ti^{2+} is -3.3eV, that of Ti^{3+} is -3.6eV and that of TiO_2^{2+} is -4.6eV.

The –F terminated multilayers have again a very large stability region, extending into acidic values of pH and for a wide range of negative potentials. The formation energy of the –OH terminated o–MXene is higher than either the –O and –F terminated structures (see Table 1). This is in contrast to the other o–MXenes considered in this study, where the –F terminated structures have the largest formation energies. The result is that the stability region of $Mo_2ScC_2(OH)_2$ is the largest of all –OH terminated MXenes considered here.

In the Pourbaix diagrams presented in Fig. 5 we have not considered ScF_3 as a possible reaction product, although there is some experimental evidence that it is present in the solution after etching.[15] If we allow the Sc atoms to react with the F atoms present in the solution, there is no region of stability for any of the solid phases (not shown). Neglecting ScF_3 as a possible reaction produce is appropriate if we assume the Sc atoms are located in internal M′ sites and are thus kinetically protected from the etching reaction. If however, some interlayer mixing is present, then this argument would

not be viable. This will be discussed further in the next section.

The formation energies of all o–MAX and o–MXene phases considered here are summarized in Table 1. In all cases, the formation energy of the MXene phase is greater than that of the associated parent phase. This explains why there is no region in phase space where the o–MAX phase remains stable in the acidic solution. It is notable that the o–MXene phases with the smallest formation energies, for example $Cr_2VC_2O_2$ with a formation energy of −6.4eV, followed by $Cr_2TiC_2O_2$ with a formation energy of −6.9eV, correspond to those with the smallest stability regions.

Interlayer mixing & Vacancies

In this section, we determine how the interlayer mixing of the metal atoms, M′ and M″, affects the Pourbaix etching diagrams of the o–MAX phases considered here.

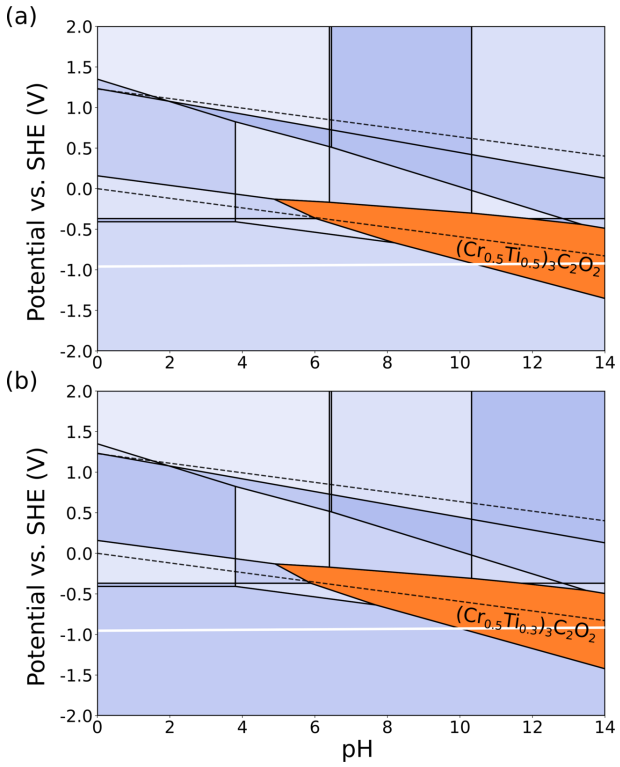

Figure 6: Etching Pourbaix diagram for $(Cr_{1/2}Ti_{1/2})_3AlC_2$ (i.e., with interlayer mixing), showing regions where (a) $(Cr_{1/2}Ti_{1/2})_3C_2O_2$ and (b) $(Cr_{1/2}Ti_{1/3})_3C_2O_2$ (i.e., with vacancies) are stable (orange segments). The dashed black lines indicate the stability range of water. The solid white line shows the point of zero charge (PZC).

The etching diagram of $(Cr_{1/2}Ti_{1/2})_3AlC_2$ is shown in Fig. 6(a). The effect of the interlayer mixing of metal atoms is to increase the stability region of the resulting oxygen-terminated o–MXene towards lower pH values (compare Fig. 6(a) to Fig. 2(a)). The PZC is also decreased from −0.6eV to −1.0eV. This increase in the stability region can be explained by an increase in the formation energy of the o–MXene structure with interlayer mixing, from −6.9eV to −8.6eV (see Table 1).

The Pourbaix etching diagram for $(Cr_{0.5}Ti_{0.3})_3C_2O_2$, i.e., an o–MXene with M′ vacancies, is shown in Fig. 6(b). The presence of vacancies has a similar effect on the area of the stability region to that of interlayer mixing, namely the o–MXene is not stable at acidic values of pH < 5.

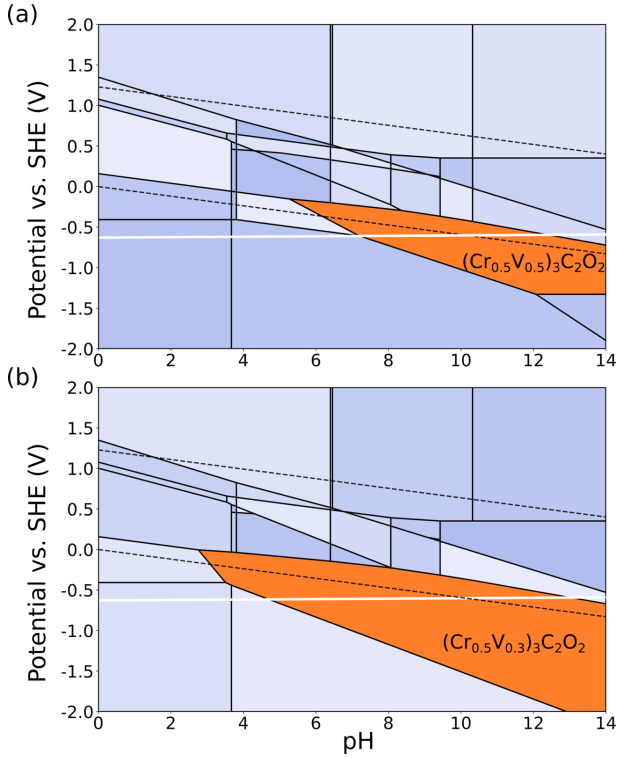

Figure 7: Etching Pourbaix diagram for $(Cr_{1/2}V_{1/2})_3AlC_2$, showing regions where (a) $(Cr_{1/2}V_{1/2})_3C_2O_2$ (i.e., with interlayer mixing) and (b) $(Cr_{1/2}V_{1/3})_3C_2O_2$ (i.e., with vacancies) are stable (orange segments). The dashed black lines indicate the stability range of water. The solid white line shows the point of zero charge (PZC).

Comparing Fig. 7(a) with Fig. 3(a) shows the increase in stability of $(Cr_{1/2}V_{1/2})_3C_2O_2$ compared to the structure with complete ordering of the metal atoms ($Cr_2VC_2O_2$). Furthermore, as the PZC is lowered from −0.41eV to −0.62eV, the o–MXene is stable when etched over a wide pH range, without the need to apply an external potential. The presence of vacancies in $(Cr_{1/2}V_{1/3})_3C_2O_2$ increases the stability region significantly compared to the $Cr_2VC_2O_2$, extending to acidic values of pH > 3 (Fig. 7(b)) at at ion concentration of 0.001 M.

If one allows for the possibility that interlayer mixing occurs in Mo_2TiAlC_2, the effect is to shift the stability region of $(Mo_{1/2}Ti_{1/2})_3C_2O_2$ to more negative potentials and higher values of pH, thereby reducing significantly the stability region. This is shown in Fig. 8(a). The relevant values of potential are outside the range of water stability, and so attempts to reach this stabil-

Table 1: Formation energies of o–MAX and o–MXene phases, calculated relative to elemental phases.

M′, M″	$M'_2M''AlC_2$	$(M'_{1/2}M''_{1/2})_3AlC_2$	$M'_2M''C_2O_2$	$(M'_{1/2}M''_{1/2})_3C_2O_2$	$(M'_{1/2}M''_{1/3})_3C_2O_2$	$M'_2M''C_2F_2$	$M'_2M''C_2(OH)_2$
Cr, Ti	-4.5	-5.1	-6.9	-8.6	-4.4	-8.7	-7.7
Cr, V	-3.9	-4.3	-6.4	-7.5	-4.1	-8.1	-7.4
Mo, Ti	-5.4	-5.9	-8.1	-9.7	-6.0	-8.4	-8.3
Mo, Sc	-4.6	-4.6	-7.4	-9.3	-5.2	-8.0	-9.9

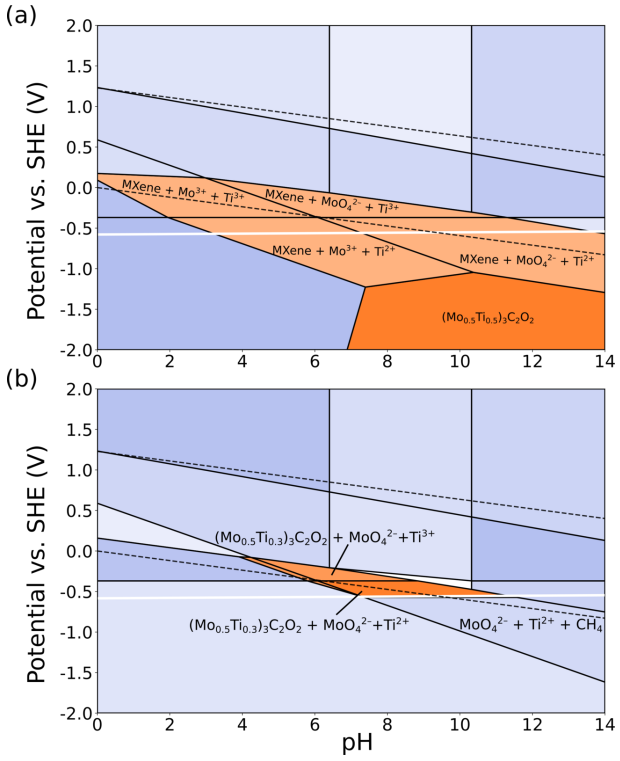

Figure 8: Etching Pourbaix diagram for $(Mo_{1/2}Ti_{1/2})_3AlC_2$, showing region where (a) $(Mo_{1/2}Ti_{1/2})_3C_2O_2$ (i.e., with interlayer mixing) and (b) $(Mo_{1/2}Ti_{1/3})_3C_2O_2$ (i.e., with vacancies) are stable (orange segments). The dashed black lines indicate the stability range of water. The solid white line shows the point of zero charge (PZC).

ity region may lead to more complex dissociation processes, not captured in the current model. However, the o–MXene is also predicted to co-exist with some of its dissolution produces including Mo^{3+} and Ti^{2+} at acidic pH values and at potentials near to the PZC of the o–MAX phase. If vacancies are considered, the stability region shrinks even further to a small region of phase space between 4 <pH< 12.

Finally, Fig. 9(a) shows the effect of including interlayer metal mixing in Mo_2ScAlC_2. Here, the stability region of the o–MXene reduces considerably to pH values greater than 10 and well below the stability region of water. Including vacancies increases it somewhat as shown in Fig. 9(b). If ScF_3 is an allowable reaction

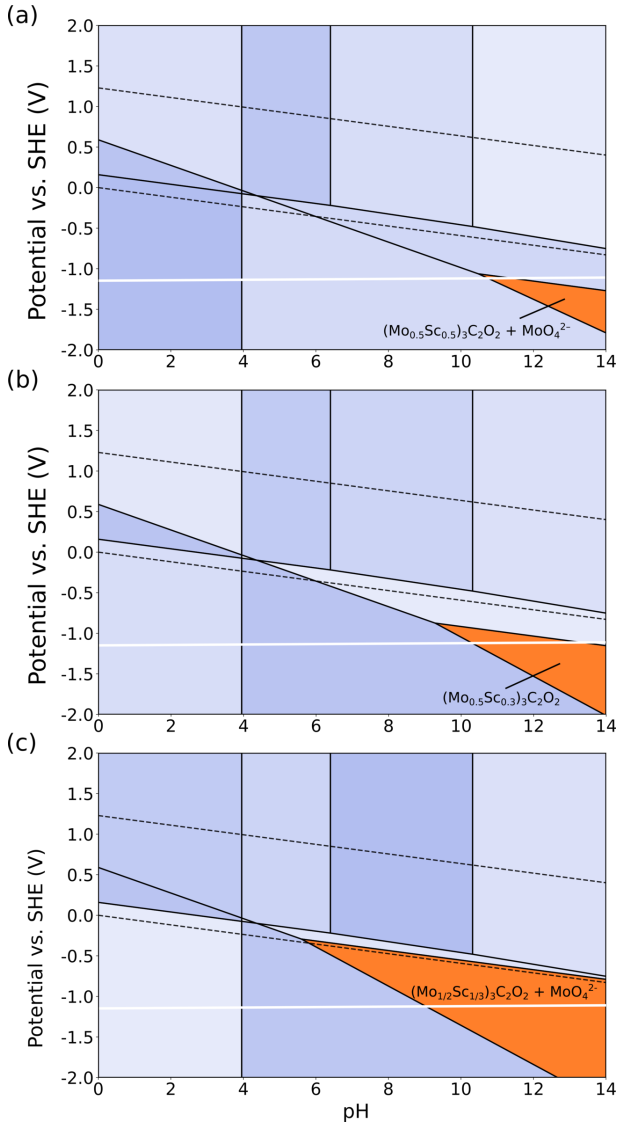

Figure 9: Etching Pourbaix diagram for $(Mo_{1/2}Sc_{1/2})_3AlC_2$ (i.e., with interlayer mixing), showing regions where (a) $(Mo_{1/2}Sc_{1/2})_3C_2O_2$ (i.e., with interlayer mixing), (b) $(Mo_{1/2}Sc_{1/3})_3C_2O_2$ (i.e., with vacancies) and (c) $(Mo_{1/2}Sc_{1/3})_3C_2O_2$ (i.e., with vacancies) at an ion concentration of 0.5 M, are stable (orange segments). The dashed black lines indicate the stability range of water. The solid white line shows the point of zero charge (PZC).

product, then again there is no region in the Pourbaix diagram where the o–MXene is stable, dissolving into ScF_3 at negative voltages where otherwise it would be considered stable (not shown). However, Pourbaix diagrams only show the thermodynamically stable outcomes, and do not take kinetic effects into account. If the Sc atoms are located only in the central layer of the M-X block it is possible that they remain trapped there, stabilizing the o–MXene at least temporally. Furthermore, increasing the ion concentration also moves the stability region of the o–MXene towards lower pH values, reaching pH values of 6 at an ion concentration of 0.5 M and moving within the water stability region (co-stable with MoO_4^{2-}). This is shown in Fig. 9(c) and can explain in some part the experimental observation of some $Mo_2ScC_2T_x$ in solution after the etching procedure.

Conclusions

Etching Pourbaix diagrams are used to predict the optimal conditions required to enhance the yields of ordered double-transition metal MXenes (o–MXenes). In agreement with experiment, we show that the experimentally observed 100% high yield of (Mo, Ti)$_2CT_x$ can be explained by a wide stability region of this o–MXene, extending into the negative pH values typical of experimental etching conditions. In contrast, (Cr, Ti)$_2CT_x$ is only stable at acidic values of pH when T_x is restricted to –F terminating groups. The same is true for (Cr, V)$_2CT_x$. (Mo, Sc)$_2CT_x$ is not stable in an aqueous acid solution if the Sc atoms can interact with the F atoms in solution to form ScF_3. If, instead, the Sc atoms are kinetically protected by being located in the inner layer, the o–MXene will be stable across a wide pH range, extending even into negative values at high ion concentrations. If, due to interlayer mixing, some Sc atoms are present in the outer o–MXene layers, they can be etched away to form ScF_3 leaving behind metal vacancies. Such multilayers are also stable in a high pH solution, with high concentrations of metallic ions in solution required to maintain stability at acidic values of pH.

Supporting Information DFT-calculated structural, electronic and magnetic properties of the o–MAX and o–MXene phases.

Acknowledgement This work was supported by a Science Foundation Ireland Starting Investigator Research Grant (15/SIRG/3314). Computational resources were provided by the supercomputer facilities at the Trinity Center for High Performance Computing (TCHPC) and at the Irish Center for High-End Computing (project tcphy091b). I would like to thank Michael Ashton for helpful discussions.

References

(1) Deysher, G.; Shuck, C. E.; Hantanasirisakul, K.; Frey, N. C.; Foucher, A. C.; Maleski, K.; Sarycheva, A.; Shenoy, V. B.; Stach, E. A.; Anasori, B. et al. Synthesis of Mo_4VAlC_4 MAX phase and two-dimensional Mo_4VC_4 MXene with 5 atomic layers of transition metals. *ACS Nano* **2020**, *14*, 204–217.

(2) Naguib, M.; Mashtalir, O.; Carle, J.; Presser, V.; Lu, J.; Hultman, L.; Gogotsi, Y.; Barsoum, M. W. Two-dimensional transition metal carbides. *ACS Nano* **2012**, *6*, 1322–1331.

(3) Anasori, B.; Xie, Y.; Beidaghi, M.; Lu, J.; Hosler, B. C.; Hultman, L.; Kent, P. R.; Gogotsi, Y.; Barsoum, M. W. Two-dimensional, ordered, double transition metals carbides (MXenes). *ACS Nano* **2015**, *9*, 9507–9516.

(4) Anasori, B.; Gogotsi, Y. *2D Metal Carbides and Nitrides (MXenes)*; Springer, 2019.

(5) Anasori, B.; Lukatskaya, M. R.; Gogotsi, Y. 2D metal carbides and nitrides (MXenes) for energy storage. *Nat. Rev. Mater.* **2017**, *2*, 16098.

(6) Li, Z.; Wu, Y. 2D early transition metal carbides (MXenes) for catalysis. *Small* **2019**, *15*, 1804736.

(7) Thakur, R.; Hoffman, M.; VahidMohammadi, A.; Smith, J.; Chi, M.; Tatarchuk, B.; Beidaghi, M.; Carrero, C. A. Multilayered two-dimensional V_2CT_x MXene for methane dehydroaromatization. *ChemCatChem* **2020**, *12*.

(8) Lee, E.; VahidMohammadi, A.; Yoon, Y. S.; Beidaghi, M.; Kim, D.-J. Two-dimensional vanadium carbide MXene for gas sensors with ultrahigh sensitivity toward nonpolar gases. *ACS Sens.* **2019**, *4*, 1603–1611.

(9) Sokol, M.; Natu, V.; Kota, S.; Barsoum, M. W. On the chemical diversity of the MAX phases. *Trends Chem.* **2019**, *1*, 210.

(10) Liu, Z.; Zheng, L.; Sun, L.; Qian, Y.; Wang, J.; Li, M. $(Cr_{2/3}Ti_{1/3})_3AlC_2$ and $(Cr_{5/8}Ti_{3/8})_4AlC_3$: new MAX-phase compounds in Ti–Cr–Al–C system. *J. Am. Ceram. Soc.* **2014**, *97*, 67–69.

(11) Liu, Z.; Wu, E.; Wang, J.; Qian, Y.; Xiang, H.; Li, X.; Jin, Q.; Sun, G.; Chen, X.; Wang, J. et al. Crystal structure and formation mechanism of $(Cr_{2/3}Ti_{1/3})_3AlC_2$ MAX phase. *Acta Mater.* **2014**, *73*, 186–193.

(12) Caspi, E. N.; Chartier, P.; Porcher, F.; Damay, F.; Cabioc'h, T. Ordering of (Cr, V) layers in nanolamellar $(Cr_{0.5}V_{0.5})_{n+1}AlC_n$ compounds. *Mater. Res. Lett.* **2015**, *3*, 100–106.

(13) Anasori, B.; Dahlqvist, M.; Halim, J.; Moon, E. J.; Lu, J.; Hosler, B. C.; Caspi, E. N.; May, S. J.; Hultman, L.; Eklund, P. et al. Experimental and theoretical characterization of ordered MAX phases Mo_2TiAlC_2 and $Mo_2Ti_2AlC_3$. *J. Appl. Phys.* **2015**, *118*, 094304.

(14) Anasori, B.; Halim, J.; Lu, J.; Voigt, C. A.; Hultman, L.; Barsoum, M. W. Mo_2TiAlC_2: A new ordered layered ternary carbide. *Scr. Mater.* **2015**, *101*, 5 – 7.

(15) Meshkian, R.; Tao, Q.; Dahlqvist, M.; Lu, J.; Hultman, L.; Rosen, J. Theoretical stability and materials synthesis of a chemically ordered MAX phase, Mo_2ScAlC_2, and its two-dimensional derivate Mo_2ScC_2 MXene. *Acta Mater.* **2017**, *125*, 476–480.

(16) Dahlqvist, M.; Rosen, J. Order and disorder in quaternary atomic laminates from first-principles calculations. *Phys. Chem. Chem. Phys.* **2015**, *17*, 31810–31821.

(17) Dahlqvist, M.; Rosen, J. Predictive theoretical screening of phase stability for chemical order and disorder in quaternary 312 and 413 MAX phases. *Nanoscale* **2020**, *12*, 785–794.

(18) Eames, C.; Islam, M. S. Ion intercalation into two-dimensional transition-metal carbides: global screening for new high-capacity battery materials. *J. Am. Chem. Soc.* **2014**, *136*, 16270–16276.

(19) Pandey, M.; Thygesen, K. S. Two-dimensional MXenes as catalysts for electrochemical hydrogen evolution: A computational screening study. *J. Phys. Chem. C* **2017**, *121*, 13593–13598.

(20) Cheng, Y.-W.; Dai, J.-H.; Zhang, Y.-M.; Song, Y. Two-dimensional, ordered, double transition metal carbides (MXenes): a new family of promising catalysts for the hydrogen evolution reaction. *J. Phys. Chem. C* **2018**, *122*, 28113–28122.

(21) Horlait, D.; Grasso, S.; Al Nasiri, N.; Burr, P. A.; Lee, W. E. Synthesis and oxidation testing of MAX phase composites in the Cr–Ti–Al–C quaternary system. *J. Am. Ceram. Soc.* **2016**, *99*, 682–690.

(22) Anasori, B.; Shi, C.; Moon, E. J.; Xie, Y.; Voigt, C. A.; Kent, P. R.; May, S. J.; Billinge, S. J.; Barsoum, M. W.; Gogotsi, Y. Control of electronic properties of 2D carbides (MXenes) by manipulating their transition metal layers. *Nanoscale Horiz.* **2016**, *1*, 227–234.

(23) Persson, K. A.; Waldwick, B.; Lazic, P.; Ceder, G. Prediction of solid-aqueous equilibria: Scheme to combine first-principles calculations of solids with experimental aqueous states. *Phys. Rev. B* **2012**, *85*, 235438.

(24) Ashton, M.; Trometer, N.; Mathew, K.; Suntivich, J.; Freysoldt, C.; Sinnott, S. B.; Hennig, R. G. Predicting the electrochemical synthesis of 2D materials from first principles. *J. Phys. Chem. C* **2019**, *123*, 3180–3187.

(25) Mathew, K.; Singh, A. K.; Gabriel, J. J.; Choudhary, K.; Sinnott, S. B.; Davydov, A. V.; Tavazza, F.; Hennig, R. G. MPInterfaces: A Materials Project based Python tool for high-throughput computational screening of interfacial systems. *Comput. Mat. Sci.* **2016**, *122*, 183–190.

(26) Ong, S. P.; Richards, W. D.; Jain, A.; Hautier, G.; Kocher, M.; Cholia, S.; Gunter, D.; Chevrier, V. L.; Persson, K. A.; Ceder, G. Python Materials Genomics (pymatgen): A robust, open-source python library for materials analysis. *Comput. Mat. Sci.* **2013**, *68*, 314–319.

(27) Kresse, G.; Furthmüller, J. Efficient iterative schemes for ab initio total-energy calculations using a plane-wave basis set. *Phys. Rev. B* **1996**, *54*, 11169.

(28) Kresse, G.; Joubert, D. From ultrasoft pseudopotentials to the projector augmented-wave method. *Phys. Rev. B* **1999**, *59*, 1758.

(29) Blöchl, P. E. Projector augmented-wave method. *Phys. Rev. B* **1994**, *50*, 17953.

(30) Perdew, J. P.; Burke, K.; Ernzerhof, M. Generalized gradient approximation made simple. *Phys. Rev. Lett.* **1996**, *77*, 3865–3868.

(31) Grimme, S.; Ehrlich, S.; Goerigk, L. Effect of the damping function in dispersion corrected density functional theory. *J. Comput. Chem.* **2011**, *32*, 1456–1465.

(32) Monkhorst, H. J.; Pack, J. D. Special points for Brillouin-zone integrations. *Phys. Rev. B* **1976**, *13*, 5188–5192.

(33) Chase Jr, M. W. NIST-JANAF thermochemical tables. *J. Phys. Chem. Ref. Data, Monograph* **1998**, *9*.

(34) Wagman, D. D.; Evans, W. H.; Parker, V. B.; Schumm, R. H.; Halow, I. *The NBS tables of chemical thermodynamic properties. Selected values for inorganic and C1 and C2 organic substances in SI units*; 1982.

(35) Pourbaix, M. *Atlas of electrochemical equilibria in aqueous solutions*; National Association of Corrosion Engineers, 1966.

(36) Mathew, K.; Kolluru, V. S. C.; Hennig, R. G. VASPsol: Implicit solvation and electrolyte model for density-functional theory. 2018; `https://github.com/henniggroup/VASPsol`.

(37) Mathew, K.; Sundararaman, R.; Letchworth-Weaver, K.; Arias, T. A.; Hennig, R. G. Implicit solvation model for density-functional study of nanocrystal surfaces and reaction pathways. *J. Chem. Phys.* **2014**, *140*, 084106.

(38) Mathew, K.; Kolluru, V. C.; Mula, S.; Steinmann, S. N.; Hennig, R. G. Implicit self-consistent electrolyte model in plane-wave density-functional theory. *J. Chem. Phys.* **2019**, *151*, 234101.

(39) Sang, X.; Xie, Y.; Lin, M.-W.; Alhabeb, M.; Van Aken, K. L.; Gogotsi, Y.; Kent, P. R.; Xiao, K.; Unocic, R. R. Atomic defects in monolayer titanium carbide ($Ti_3C_2T_x$) MXene. *ACS Nano* **2016**, *10*, 9193–9200.

(40) Persson, P. O.; Rosen, J. Current state of the art on tailoring the MXene composition, structure, and surface chemistry. *Curr. Opin. Solid State Mater. Sci.* **2019**, *23*, 100774.

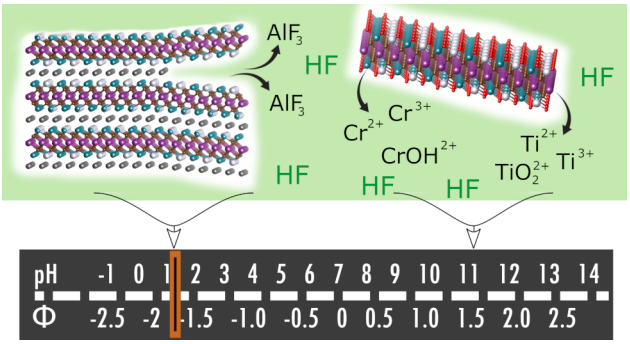

Figure 10: TOC Graphic